

Semi-automatic segmentation of subcutaneous tumours from micro-computed tomography images

This content has been downloaded from IOPscience. Please scroll down to see the full text.

2013 Phys. Med. Biol. 58 8007

(<http://iopscience.iop.org/0031-9155/58/22/8007>)

View [the table of contents for this issue](#), or go to the [journal homepage](#) for more

Download details:

IP Address: 139.179.103.108

This content was downloaded on 04/11/2013 at 06:41

Please note that [terms and conditions apply](#).

Semi-automatic segmentation of subcutaneous tumours from micro-computed tomography images

Rehan Ali¹, Cigdem Gunduz-Demir², Tünde Szilágyi³, Ben Durkee¹
and Edward E Graves¹

¹ Department of Radiation Oncology, Stanford University, Stanford, CA, USA

² Department of Computer Engineering, Bilkent University, Ankara, Turkey

³ Department of Engineering Science, University of Oxford, Oxford, UK

E-mail: egraves@stanford.edu

Received 28 June 2013, in final form 19 September 2013

Published 30 October 2013

Online at stacks.iop.org/PMB/58/8007

Abstract

This paper outlines the first attempt to segment the boundary of preclinical subcutaneous tumours, which are frequently used in cancer research, from micro-computed tomography (microCT) image data. MicroCT images provide low tissue contrast, and the tumour-to-muscle interface is hard to determine, however faint features exist which enable the boundary to be located. These are used as the basis of our semi-automatic segmentation algorithm. Local phase feature detection is used to highlight the faint boundary features, and a level set-based active contour is used to generate smooth contours that fit the sparse boundary features. The algorithm is validated against manually drawn contours and micro-positron emission tomography (microPET) images. When compared against manual expert segmentations, it was consistently able to segment at least 70% of the tumour region ($n = 39$) in both easy and difficult cases, and over a broad range of tumour volumes. When compared against tumour microPET data, it was able to capture over 80% of the functional microPET volume. Based on these results, we demonstrate the feasibility of subcutaneous tumour segmentation from microCT image data without the assistance of exogenous contrast agents. Our approach is a proof-of-concept that can be used as the foundation for further research, and to facilitate this, the code is open-source and available from www.setuvo.com.

(Some figures may appear in colour only in the online journal)

1. Introduction

X-ray computed tomography (CT) is a commonly used technique for acquiring *in vivo* 3D volumetric images. The images are formed by the attenuation of x-rays as they pass through the object, and provide clear information regarding internal anatomical structures wherever there are strong differences in linear attenuation coefficient (which is dependent on material

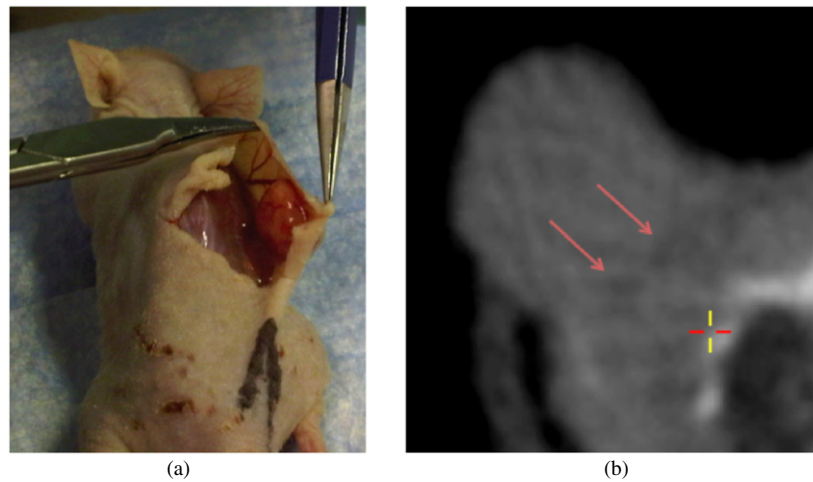


Figure 1. (a) A shoulder-borne subcutaneous tumour being cut away from the mouse body. The tumour is a self-contained mass which does not invade into the underlying muscle. (b) An axial microCT slice of the tumour exhibiting faint dark features at the tumour–muscle boundary (highlighted with red arrows).

density and atomic number). CT images are able to identify certain types of pathology such as lung tumours, where the tumours are clearly visible against a background of air-filled lung tissue, but they are well known to lack soft tissue contrast, and this limits their ability to differentiate most internal tissues.

Murine subcutaneous tumour models are a mainstay of preclinical oncology research. They involve solid tumours grown between the skin and muscle, and provide simple models for evaluating the efficacy of new therapeutics. Subcutaneous tumours are frequently imaged with a combination of positron emission tomography (PET) and CT using integrated PET/CT scanners. The PET image data provides *in vivo* images of specific biological processes, such as metabolism or hypoxia, occurring within the tumour. Tumour-specific PET signals are frequently produced by a biologically active subset of cells within the tumour, but the biologically inactive cells are indistinguishable from normal tissue, and this makes it difficult to quantify the proportion of PET-positive and negative tumour cells within the tumour. The CT data provides an anatomic reference for the PET data, and in theory it could yield an accurate tumour boundary to superimpose over the PET data. In practice the tumour–muscle interface is hard to delineate due to the lack of soft tissue contrast, and as a result this is rarely done except by manually performed segmentations. Partially automated subcutaneous tumour segmentation has been demonstrated using contrast-enhanced flat-panel detector CT (Missbach-Guentner *et al* 2008) and T2-weighted MRI (Montelius *et al* 2012), however to our knowledge, there has been no prior work on using image processing to segment subcutaneous tumours using non-contrast CT images.

In this paper we describe a semi-automatic algorithm for segmenting the boundary of murine subcutaneous tumours from microCT image data, which is able to locate the tumour–muscle interface. Our method does not use any exogenous contrast agent, and can work using attenuation corrected CT scans which accompany PET images on integrated PET/CT scanners. It relies on the presence of faint features at the tumour–muscle interface which are a result of the tumour being separated from the muscle by a thin layer of blood vessels and connective membranes. This layer, which is less dense than the surrounding tissue, can be observed as slightly dark regions in microCT images (figure 1). By using an intensity-invariant

feature detection method to emphasize these features, along with an active contour with a strong smoothness constraint, it is possible to develop an algorithm that can automatically segment the tumour boundary.

The algorithm described in this paper is validated against manual segmentations and microPET images. The complete open-sourced application, along with videos demonstrating the method, can be found at www.setuvo.com.

2. Materials and methods

2.1. Image acquisition

Animal studies were approved by the Administrative Panel for Lab Animal Care (APLAC) at Stanford University. For subcutaneous tumours, 6 week old male nude mice were injected with 1 million A549 human lung carcinoma tumour cells under the skin of each shoulder, and tumours were grown for six weeks. For orthotopic breast tumours, 1 million MDA-MB-231 human breast adenocarcinoma cells were injected into the mammary fat pads of 6 week old female mice. Tumors were grown for eight weeks prior to imaging.

For imaging, animals were injected with 7.5 MBq of ^{18}F -EF5 or ^{18}F -FAZA via tail vein injection and imaged three hours later. Following anaesthetization using 2% isoflurane, mice were imaged with a Siemens Inveon microPET/CT. An attenuation correction CT scan was first acquired, followed by a 10 min PET scan. The microCT datasets were reconstructed using a Filtered Back Projection algorithm to a resolution of $480 \times 480 \times 632$, with a voxel length of 0.21 mm in each axis. The PET list mode data was binned into a single frame and reconstructed using an OSEM (ordered-subsets expectation maximization) algorithm to a resolution of $128 \times 128 \times 159$, with a voxel length of 0.77 mm in the x and y axes, and 0.79 mm in the z axis.

2.2. Pre-processing

Two thresholds were applied to the microCT data $I(x, y)$. The threshold t_a to separate tissue from air, and t_b to separate tissue from bone. The bone map obtained by thresholding with t_b was subjected to a morphological dilation which expanded the bone regions by two voxels in all directions, yielding a binary map I_{bone} . An exclusion map, I_{ex} , is constructed using the equation

$$I_{\text{ex}} = \begin{cases} 1 & \text{if } I_{\text{bone}} = 1 \\ 1 & \text{if } I < t_a \\ 0 & \text{otherwise.} \end{cases} \quad (1)$$

A sample exclusion map is shown in figure 2(b).

2.3. Local phase feature detection

Local phase is a commonly used concept for detecting features in 1D signal processing in an intensity-invariant manner. A suitably chosen even bandpass filter, $b_e(t)$, and its Hilbert Transform, $b_o(t)$, which is odd, can be applied to a signal $f(t)$ to yield information on its shape (local phase, φ) and magnitude (local energy) at any given point. The local phase of a 1D signal $f(t)$ is defined in Boukerroui *et al* (2004) as

$$\varphi(t) = \arctan \left(\frac{b_e(t) \otimes f(t)}{b_o(t) \otimes f(t)} \right) \quad (2)$$

and describes the differential response of the signal to the odd and even filters (figure 3). The result is a measure of the odd or even symmetry of the localized signal feature. This principle

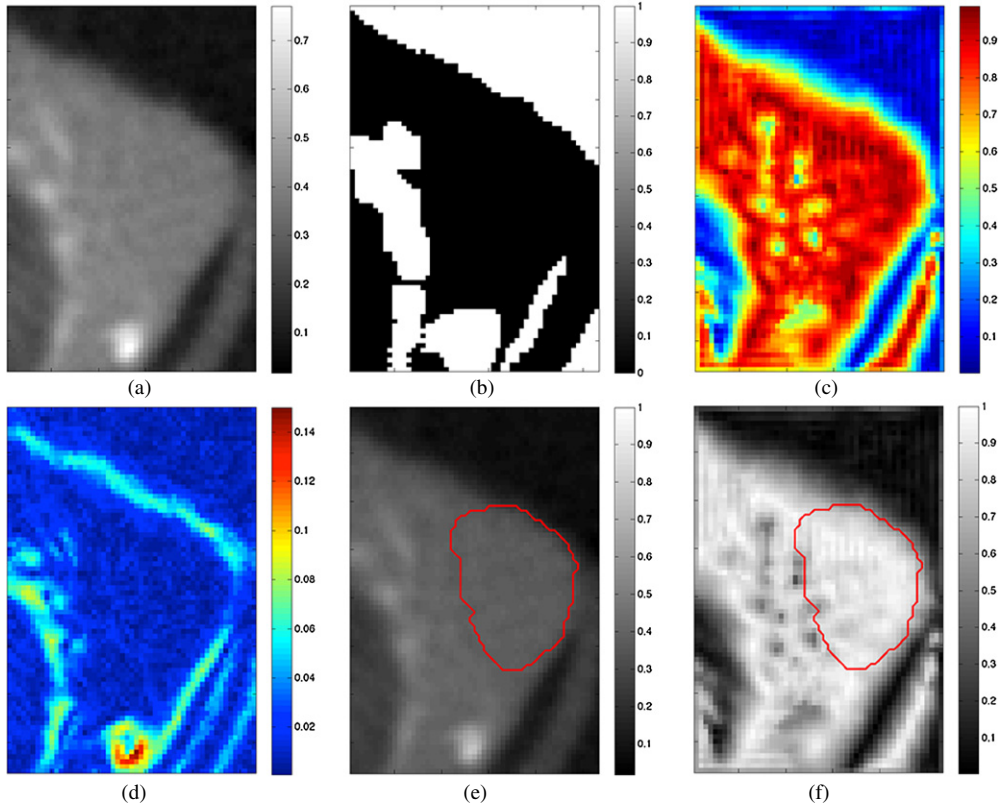


Figure 2. (a) Axial microCT slice of subcutaneous tumour. (b) Exclusion map highlighting air and bone (white regions). (c) Local phase map highlighting faint boundary features (yellow spots). (d) Gradient map. ((e), (f)) Segmentation result from algorithm (red contour) superimposed on microCT image (e) and local phase map (f).

can be extended to multiple dimensions using Felsberg's Monogenic Signal framework (Felsberg and Sommer 2001), where it is used as an intensity-invariant image-based feature detector.

The bandpass filter is generated using a rotationally invariant filter (Mellor and Brady 2005),

$$b_e(r) = \frac{1}{r^{\alpha+\beta}} - \frac{1}{r^{\alpha-\beta}} \quad (3)$$

where $\alpha = 3.25$ and $\beta = 0.25$. Using this, local phase φ is computed as described in Mellor and Brady (2005), using the equation

$$\varphi(x, y) = \arctan \left(\frac{I \otimes b_e}{\sqrt{(h_1 \otimes (I \otimes b_e))^2 + (h_2 \otimes (I \otimes b_e))^2}} \right) \quad (4)$$

where I is the image, b_e is the even bandpass filter, and h_1, h_2 are vector-valued filters which generate a quadrature pair of odd filters when convolved with the even bandpass filter. These vector-valued filters are generated using an extension of the Hilbert transform known as

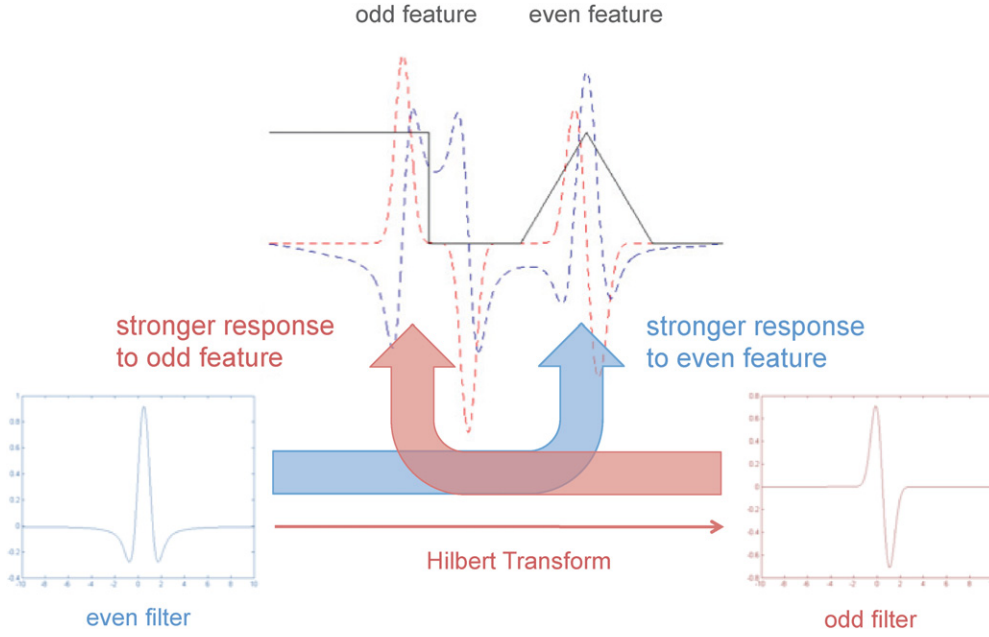


Figure 3. Local phase relies on the differential response of odd and even filters to odd and even symmetric features. A 1D signal (black line) is shown containing an odd feature (step function) and an even feature (triangle function). When an even 1D difference of Gaussians filter is convolved with the signal, the output (blue dashed line) is stronger for the even feature. The Hilbert Transform is used to generate a quadrature odd filter from the initial even filter, and this yields a stronger response to the odd feature (red dashed line).

the Reisz transform (Felsberg and Sommer 2001), and they enable the generation of higher dimension odd filters. In the 2D frequency domain, these filters are defined as

$$H_1(u_1, u_2) = i \frac{u_1}{\sqrt{u_1^2 + u_2^2}} \quad (5)$$

$$H_2(u_1, u_2) = j \frac{u_2}{\sqrt{u_1^2 + u_2^2}} \quad (6)$$

where u_1, u_2 are the spatial frequencies resulting from the 2D Fourier transform of $I(x, y)$.

The Felsberg formalism is naturally extensible to higher dimensions, which is useful for our current application. Wang *et al* defined 3D local phase as

$$\varphi(x, y) = \arctan \left(\frac{I \otimes b_e}{\sqrt{(h_1 \otimes (I \otimes b_e))^2 + (h_2 \otimes (I \otimes b_e))^2 + (h_3 \otimes (I \otimes b_e))^2}} \right) \quad (7)$$

where h_1, h_2, h_3 are the transfer functions of

$$H_1(u_1, u_2, u_3) = i \frac{u_1}{\sqrt{u_1^2 + u_2^2 + u_3^2}} \quad (8)$$

$$H_2(u_1, u_2, u_3) = j \frac{u_2}{\sqrt{u_1^2 + u_2^2 + u_3^2}} \quad (9)$$

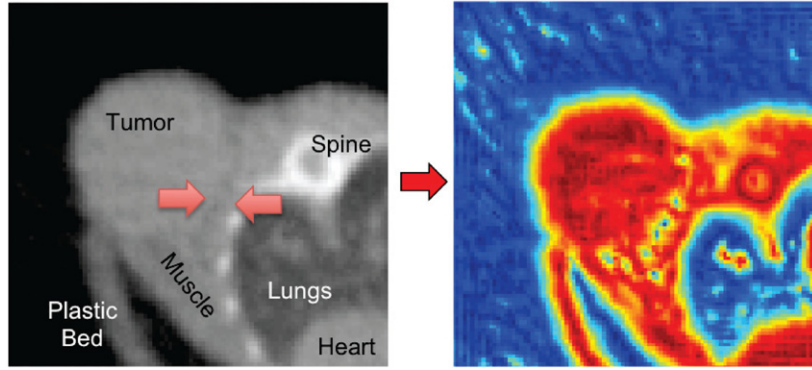


Figure 4. An axial microCT slice of a subcutaneous tumour (left), and its corresponding local phase map (right). The faint interface features highlighted with red arrows on the microCT image are emphasized in the local phase image as yellow/blue dots.

$$H_3(u_1, u_2, u_3) = k \frac{u_3}{\sqrt{u_1^2 + u_2^2 + u_3^2}} \quad (10)$$

thus allowing local phase to be computed on volumetric data (Wang *et al* 2009). Figure 4 shows the local phase map for a single slice from a microCT volume, and it can be seen that faint features at the interface between the tumour and body are highlighted in blue.

2.4. Level set segmentation

A 3D level set is used to segment the tumour boundary using a combination of the local phase and exclusion maps, based on the implementations described in Lefohn *et al* (2004) and Mostofi (2009). A signed distance function ϕ is initialized using a user input click within the tumour volume, and this is evolved using the level set PDE

$$\frac{\partial \phi}{\partial t} = -\|\nabla \phi\| \left[\alpha F + (1 - \alpha) \nabla \cdot \frac{\nabla \phi}{\|\nabla \phi\|} \right] \quad (11)$$

where α is a weighting coefficient for the two terms. The second term defines the regularizing curvature term, which enforces a smoothness constraint on the boundary. The F term within the bracket describes an image-based speed term where

$$F = \begin{cases} \epsilon - |\varphi - T| + \beta \nabla I & \text{if } I_{\text{ex}} = 0 \\ 0 & \text{otherwise} \end{cases} \quad (12)$$

where φ is the local phase map (equation (7)), T defines a target threshold local phase value, ϵ defines a margin around that threshold, I_{ex} is the thresholded microCT image defined in equation (1) and β is a weighting factor for the gradient term. If the level set boundary lies on a voxel whose local phase value lies within $(T - \epsilon) < T < (T + \epsilon)$ then it will experience a positive growth force at that point, otherwise it will experience a negative shrinking force. The exclusion map I_{ex} causes the level set to experience no force if it ventures out into the excluded regions (air and bone). In these instances, it will undergo smoothing (and a slight amount of shrinkage) due to the curvature term. The gradient term is used because the local phase of the tumour–muscle interface features are of a similar value to the tumour–air perimeter voxels, and therefore the speed term is boosted in this region to encourage the level set to extend to the tumour–air boundary. A sample gradient map is shown in figure 2(d).

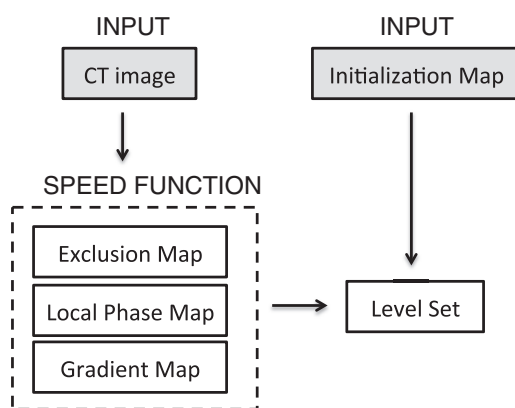


Figure 5. Outline of segmentation algorithm.

Table 1. Summary of parameters for the CT tumour segmentation algorithm. MicroCT data and local phase maps are normalized to range 0–1.

Parameter	Symbol	Approximate value
CT air threshold	t_a	0.1
CT bone threshold	t_b	0.9
Level set weighting	α	0.65
Local phase margin	ϵ	0.15
Local phase threshold	T	0.9
Gradient map contribution	β	5.0

The level set equation is solved in C using upwind differencing (Osher and Fedkiw 2002) and the narrow-band implementation described by Lefohn *et al* (2004). The parameters used are shown in table 1. Most of the parameters are determined via observation of the microCT image and local phase data values for the boundary features, however optimization is performed for α and β by comparing outputs for a range of values ($0.55 < \alpha < 0.75$ and $0 < \beta < 10$). The segmentation algorithm is written in Matlab using a GUIDE-based interface for simple user operation, and the level set is called through a MEX function. The whole algorithm is summarized in figure 5.

2.5. Validation

The segmentation results are assessed by comparison against manually segmented tumours. The manual contours were drawn by a radiation oncology resident with experience in CT tumour segmentation, using image features that defined the surgical flat plane (the interface between the tumour and muscle tissue layers). Each manual segmentation is accompanied with a confidence value between 1–5 which represents the resident’s confidence in identifying the correct boundary. Low confidence values of 1–2 were due to small or irregular tumours with few flat plane features, or tumours that were proximal to a forelimb. High values of 4–5 were due to large tumours and/or excellent flat plane features. The software used for manual contouring was Amira 5.4.3 software (Visualization Sciences Group, Burlington, MA, USA).

The Dice similarity metric (Dice 1945) is computed to determine the level of agreement between the algorithm output and the manually drawn tumour boundaries. Given two segmentation regions A and B , the Dice measure is given by

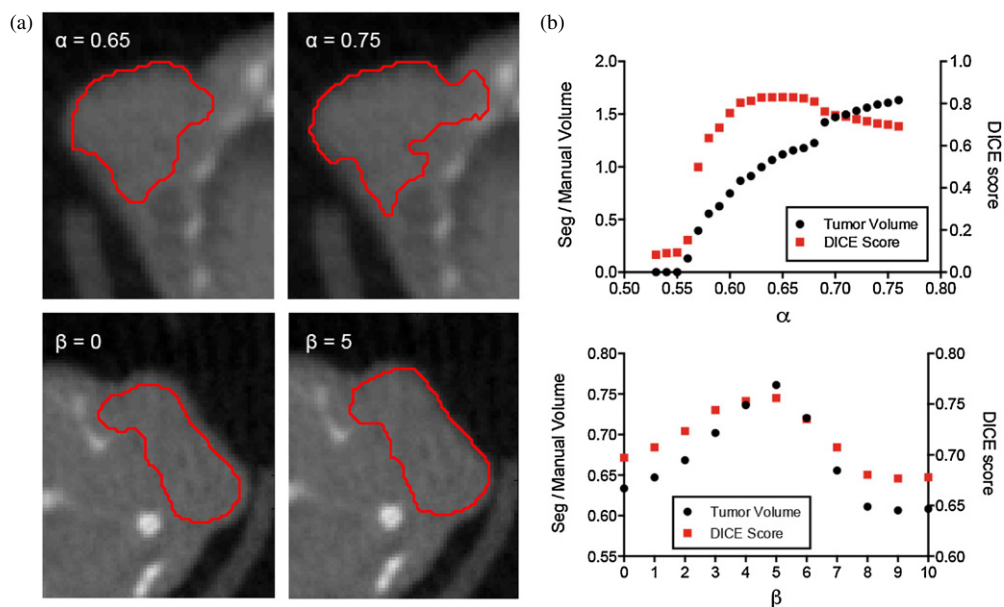


Figure 6. (a) Images showing the effect of varying α and β . (top row) Effect of varying α in equation (11). If α is too high then the level set spills out into the neighbouring tissue. (bottom row) Effect of varying β in equation (12). If β is too low then the level set does not extend all the way to the tumour–air boundary. (b) Plots of α and β against relative tumour volume (segmentation volume/manually drawn volume) and Dice score for parameter optimization.

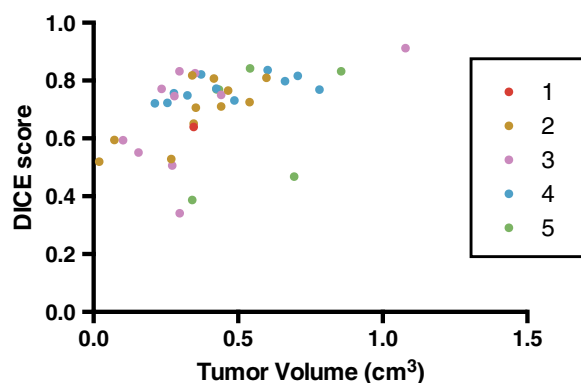


Figure 7. Evaluation of segmentation results against manual segmentations using DICE scores. Each tumour is colour-coded according to the confidence of the resident in drawing the boundaries. Scores range from 1 (low confidence) to 5 (high confidence).

$$D(A, B) = \frac{2n(A \cap B)}{n(A) + n(B)} \quad (13)$$

where $n(\cdot)$ represents the number of voxels included in a region. The Dice measure produces values between 0 and 1, where 1 represents perfect overlap.

Segmentation boundaries were also compared against co-acquired (and co-registered) ¹⁸F-EF5 microPET images. The tumour microPET signal was automatically segmented by a 3D region growing algorithm. A manually placed seed point was used to grow out a continuous region up to a fixed intensity threshold $T_{PET} = 1.5(I_{muscle})$, where I_{muscle} is by the mean PET

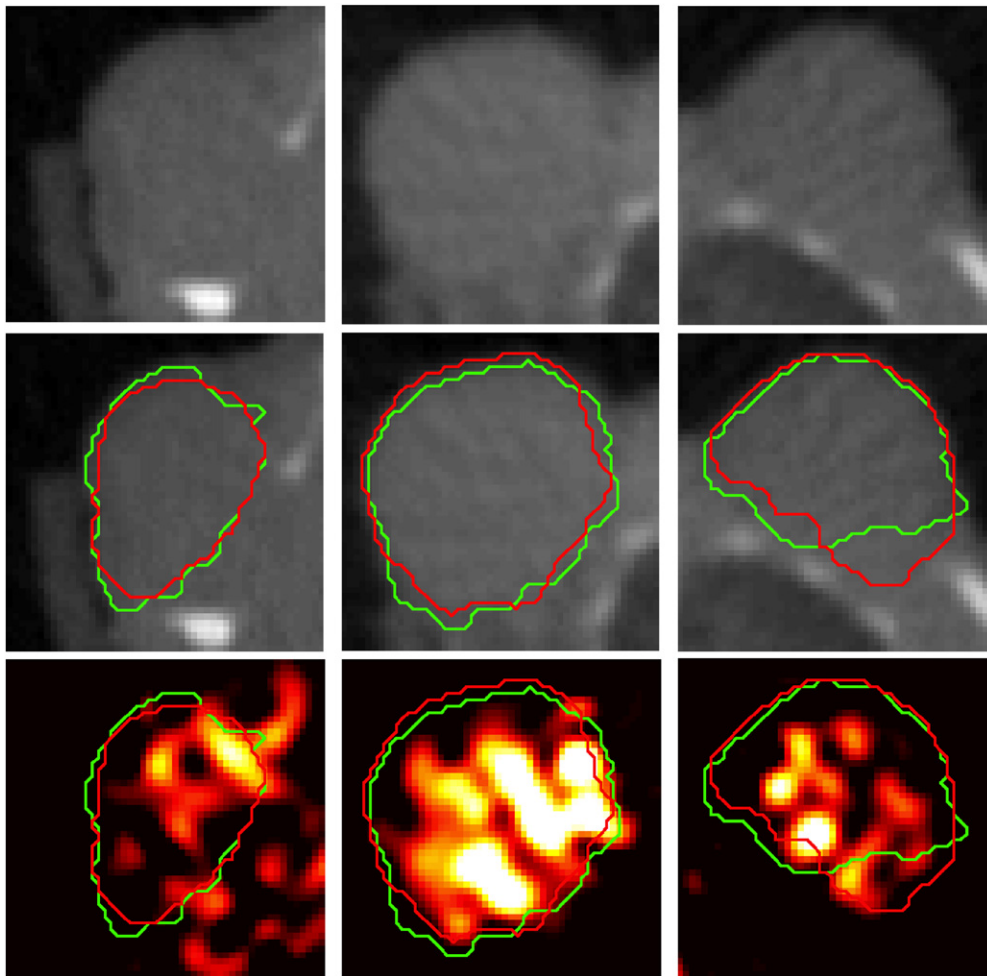


Figure 8. Comparison between segmentation results (red contour) against manual segmentations (green contour) and tumour PET tracer uptake for three different A549 subcutaneous tumours (one per column). Top row shows axial microCT slices of the tumour. Middle row shows the same slice with the segmentation contours superimposed. Bottom row shows co-registered PET image of ^{18}F -EF5 uptake in the tumours, with segmentation contours superimposed.

intensity (defined as % injected dose per unit volume) in a reference muscle. This approach mimics the approach used clinically in defining hypoxic regions from hypoxia PET tracer data using a tumour–muscle ratio of 1.5 (Komar *et al* 2008).

3. Results

Figure 2 shows the output from each step of the algorithm. The white regions in the exclusion map (figure 2(b)) dictate no-go areas for the level set. The local phase map (figure 2(c)) shows the tumour and tissue in red ($0.8 \leq \varphi \leq 0.95$), and the level set parameters ϵ and T are set to grow in these regions. The interface features are represented in the local phase map as blue regions ($\varphi \leq 0.6$). The tumour–air boundary voxels have similar local phase values ($0.5 \leq \varphi \leq 0.7$), corresponding to the relatively dark layer of tumour voxels on the

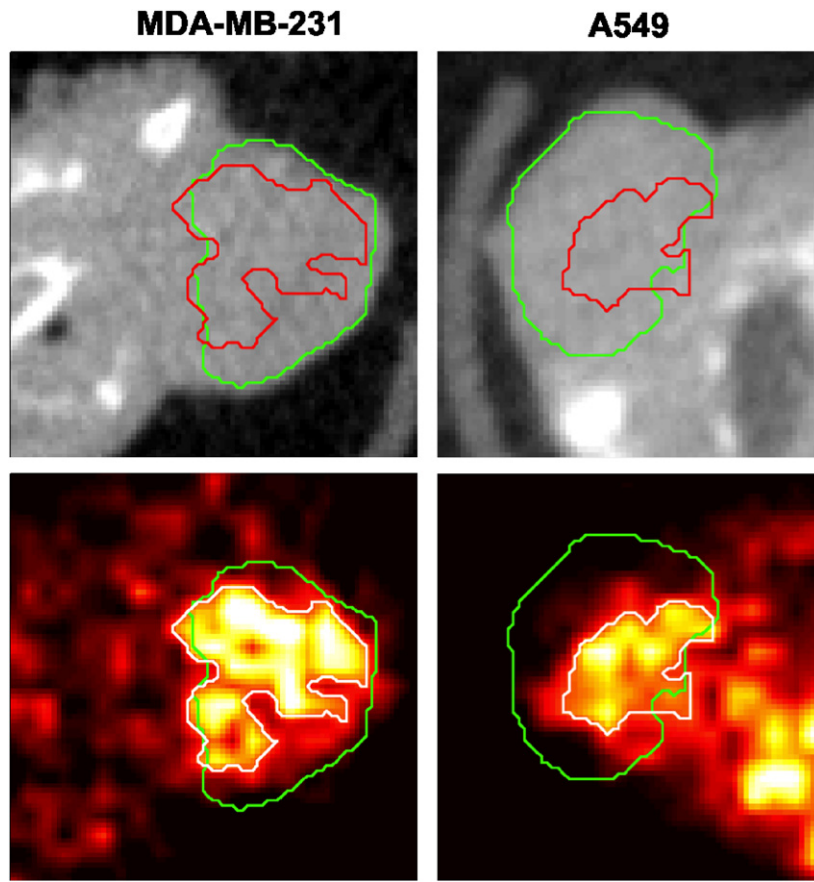


Figure 9. Comparison between the CT tumour segmentation result (green contour) and a region growing algorithm for segmenting the tumour PET signal (red contour in top CT image, white contour in bottom PET image). Top row shows axial microCT slices of the tumour, and bottom row shows co-registered PET image. Left column shows ^{18}F -FAZA uptake in an orthotopic MDA-MB-231 tumour, and right column shows ^{18}F -EF5 uptake in an A549 subcutaneous tumour.

Table 2. Quantitation of percentage of functional tumour microPET region captured by CT tumour segmentation, and size of tumour microPET region as a percentage of the microCT-derived volume. n represents number of tumours analysed.

Tumour type	Tracer	% PET region captured	Fraction of CT volume	n
A549	^{18}F -EF5	87.9 ± 2.7	37.8 ± 13.7	15
MDA-MB-231	^{18}F -FAZA	81.8 ± 15.1	63.1 ± 24.1	8

air boundary due to partial volume effect, and this causes the level set to terminate early. To counteract this, the gradient map (figure 2(d)) is added to the local phase map to raise the values of the air boundary voxels, thus encouraging the level set to propagate to the true boundary.

Figures 2(e) shows the results of the level set (red contour) superimposed over the original microCT image, and figure 2(f) shows the level set result superimposed on the local phase map. The level set is clearly arrested when it encounters the local phase boundary features, and the curvature term prevents it from leaking out from the edges where fewer features are available.

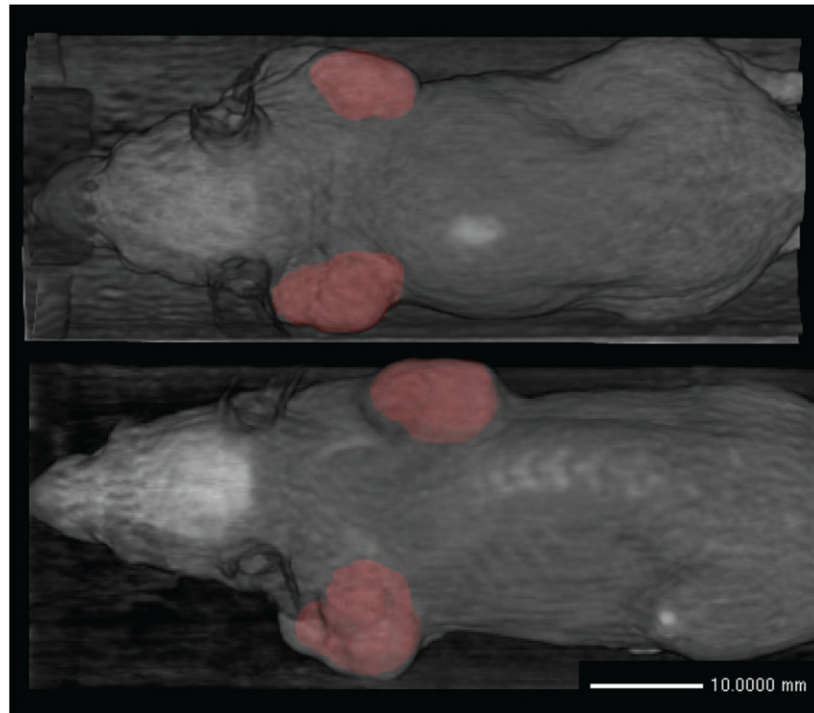


Figure 10. Birds-eye view 3D volume rendering of the segmentation results (red) superimposed on the microCT image (grey) for two mice.

The effect of the key parameters is shown in figure 6. Two parameters are optimized, α in equation (11) and β in equation (12). The most important term is α , the speed function tuning parameter which determines the relative contribution of the local phase map and the curvature term. When α is too high, the local phase term dominates and the level set spills out into the neighbouring tissues. Conversely, when α is too low, the curvature term dominates and the level set undergoes a net shrinkage. The plot in figure 6(b) shows that α is relatively insensitive to small variations around the optimal value ($\alpha \pm 0.05$), but the segmentation quality degrades rapidly outside this range. The second term, β , controls the gradient map weight. When β is close to zero, the level set does not reach the tumour–air boundary. The optimum value is found around $\beta = 5$, although the algorithm is relatively insensitive to variations in β . The parameter values in table 1 were found to work with most of the analysed tumours, with minor variations in α yielding improvements in some cases.

Figure 7 summarizes the segmentation results against manual segmentations ($n = 39$) for A549 subcutaneous tumours. When compared against manual segmentations, the algorithm achieves consistently high Dice scores (mean Dice score is 0.71; 95% confidence interval is 0.67–0.75) across a range of tumour volumes (range 0.1–1.1 cm³). The algorithm is able to perform well in simple and difficult cases (as determined by the resident’s confidence in each contour). Six tumours obtain Dice scores less than 0.5. Examination of these tumours reveals two causes of the low scores. The first is that the algorithm underestimates the manually drawn boundary, and in the case of small tumours, this results in a higher proportion of false-negative voxels which impacts the score. The second is that the level set overshoot the true boundary due to a lack of strong tumour–tissue interface features to constrain it.

Figure 8 shows the manual and level set boundaries compared for three different tumours, against both the microCT and the ^{18}F -EF5 microPET image data. The manual and level set boundaries show good overall agreement, and both are able to capture most of the tumour-specific microPET tracer signal. Figure 9 shows a comparison between the level set contour and a region growing algorithm boundary designed to capture the functional tumour microPET signal. The hypoxia microPET signal highlights a functional subvolume of the tumour, however the microCT tumour algorithm is able to capture most of this subvolume. Table 2 summarizes the extent to which the microCT boundary is able to capture the tumour microPET functional volume. The algorithm is able to capture 88% of tumour microPET signal in A549 tumours, which tend to have small functional volumes (38% of the overall tumour volume), and slightly less (82%) for orthotopic MDA-MB-231 tumours which have larger functional volumes (63% of the overall tumour volume).

Figure 10 shows a 3D rendering of mice with multiple segmented tumours. The level set takes 30 s to compute 1000 iterations on a 2010 Macbook Pro with a 2.4 GHz Intel Core i5 and 4 GB DDR3 RAM. It typically takes 1500–1800 iterations to reach convergence for a single tumour.

4. Discussion

PET images require some form of anatomic reference in order to make full use of the available biological information. Modern PET/CT scanners produce high resolution anatomic CT images which are co-registered with the PET images, and such scanners are becoming widely used for animal research. For certain types of tumours, particularly lung tumours, CT images allow tumour boundaries to be directly observed and segmented (Fushiki *et al* 2009). Subcutaneous tumours are one of the most widely used preclinical cancer models (Sausville and Burger 2006), however the boundary at the muscle interface is hard to discern due to the low soft tissue contrast in CT. Other modalities such as MRI and ultrasound are better able to distinguish tumour tissue from the neighbouring muscle, and these methods are sufficient for measuring tumour volumes (Montelius *et al* 2012, Ayers *et al* 2010), however they are difficult to register to PET data.

Segmenting subcutaneous tumour boundaries from microCT images is a difficult image processing problem, and there exists little prior work in this area. Missbach-Guentner *et al* (2008) proposed a method which used intravenous contrast to highlight the tumour vasculature, which in subcutaneous tumours is peripheral to the tumour tissue. This would make segmentation more amenable to straightforward image processing techniques. To our knowledge, there exists no partially automated method for segmenting such tumours from microCT images without any exogenous contrast. Our work provides a first proof-of-principle to demonstrate the feasibility of solving this problem.

Our approach uses a biological feature of subcutaneous tumours, namely their inability to invade into the underlying tissue. They form compact solid blocks of tissue which are fed by the host's vascular system, and the development of these peripheral blood vessels results in the formation of a thin membrane which separates the tumour from the muscle. This can be observed in microCT images in the form of sparse faint dark features. In order to utilize these features, we employ two techniques. The first is local phase based feature detection which emphasizes the faint boundary features in a way that is insensitive to variations in image intensity/contrast (by focusing on the line symmetry of the local signal). The second is a level set active contour which regularizes the problem through the use of a smoothness constraint, thus overcoming the feature sparsity problem. The method shows promising results on two tumour types (human A549 lung carcinoma cell and MDA-MB-231 breast adenocarcinoma

xenografts) and a single scanner (a Siemens Inveon microPET/CT). Further development of this method will require testing on different tumour types and images from different scanners.

The algorithm is available as open-source software from www.setuvo.com. There exists considerable scope for improvements. GPU-based techniques can be used to improve the speed of the level set computation, and the initialization methods can also be improved (using, for example, co-acquired PET data). The accuracy can be improved through the incorporation of additional prior information based on an improved understanding of the tumour models being imaged. Our future work involves using the segmentation boundaries as an input for mathematical models of tumour growth, thus providing tumour boundary conditions for the models. Other uses can include the development of PET tumour quantification metrics which include the contribution from PET-negative tumour voxels, for example tumour hypoxic fraction when imaging with hypoxia-specific PET tracers.

Acknowledgments

The authors would like to thank the funding providers which include the Stanford Molecular Imaging Scholars program (NIH/NCI R25 CA118681-06) which funded RA, and NIH/NCI R01 CA131199 which funded the imaging studies.

References

- Ayers G D *et al* 2010 Volume of preclinical xenograft tumors is more accurately assessed by ultrasound imaging than manual caliper measurements *J. Ultrasound Med.* **29** 891–901
- Boukerroui D, Brady M and Noble A 2004 On the choice of band-pass quadrature filters *J. Math. Imaging Vis.* **21** 53–80
- Dice L 1945 Measures of the amount of ecologic association between species *Ecology* **26** 297–302
- Felsberg M and Sommer G 2001 The monogenic signal *IEEE Trans. Signal Process.* **49** 3136–44
- Fushiki H, Kanoh-Azuma T, Katoh M, Kawabata K, Jiang J, Tsuchiya N, Satow A, Tamai Y and Hayakawa Y 2009 Quantification of mouse pulmonary cancer models by microcomputed tomography imaging *Cancer Sci.* **100** 1544–9
- Komar G, Seppänen M, Eskola O, Lindholm P, Grönroos T J, Forsback S, Sipilä H, Evans S M, Solin O and Minn H 2008 18F-EF5: a new PET tracer for imaging hypoxia in head and neck cancer *J. Nucl. Med.* **49** 1944–51
- Lefohn A E, Kniss J M, Hansen C D and Whitaker R T 2004 A streaming narrow-band algorithm: interactive computation and visualization of level sets *IEEE Trans. Vis. Comput. Graphics* **10** 422–33
- Mellor M and Brady M 2005 Phase mutual information as a similarity measure for registration *Med. Image Anal.* **9** 330–43
- Missbach-Guentner J, Dullin C, Tomography C, Kimmina S, Zientkowska M, Domeyer-Missbach M and Malz C 2008 Morphologic changes of mammary carcinomas in mice over time as monitored by flat-panel detector volume *Neoplasia* **10** 663–73
- Montelius M, Ljungberg M, Horn M and Forssell-Aronsson E 2012 Tumour size measurement in a mouse model using high resolution MRI *BMC Med. Imaging* **12** 12
- Mostofi H 2009 Fast level set segmentation of biomedical images using graphics processing units *PhD Thesis* University of Oxford, UK
- Osher S and Fedkiw R 2002 *Level Set Methods and Dynamic Implicit Surfaces* (Berlin: Springer)
- Sausville E A and Burger A M 2006 Contributions of human tumor xenografts to anticancer drug development *Cancer Res.* **66** 3351–4 (discussion 3354)
- Wang P, Kelly C and Brady M 2009 Application of 3D local phase theory in vessel segmentation *ISBI'09: 6th IEEE Int. Symp. on Biomedical Imaging* pp 1174–7